Records of volcanism and organic carbon isotopic composition (13Corg) linked to changes in atmospheric pCO2 and climate during the Pennsylvanian icehouse interval

Lu, Jing; Wang, Ye; Yang, Minfang; Shao, Longyi; Hilton, Jason

[Link to publication on Research at Birmingham portal](#)

Records of volcanism and organic carbon isotopic composition ($\delta^{13}C_{org}$) linked to changes in atmospheric pCO$_2$ and climate during the Pennsylvanian icehouse interval

Jing Lu [a], Ye Wang [a], Minfang Yang [b], Longyi Shao [a], Jason Hilton [c,*]

[a] *State Key Laboratory of Coal Resources and Safe Mining, College of Geoscience and Surveying Engineering, China University of Mining and Technology, Beijing 100083, PR China*
[b] *Petroleum Exploration and Development Research Institute, PetroChina, Beijing 100083, PR China*
[c] *School of Geography, Earth and Environmental Sciences, University of Birmingham, Edgbaston, Birmingham B15 2TT, UK*

ABSTRACT

The late Paleozoic ice age (LPIA) during the Carboniferous and Permian (ca. 360–260 Ma) was vegetated Earth's only recorded icehouse-to-greenhouse transition and provides a deep-time perspective for climate-glaciation-environment coevolution and future climate change. During the LPIA, changes in glacial-interglacial cycles have been closely linked to atmospheric pCO$_2$. In this paper, we investigate the relationship between volcanism and glacial to interglacial climate cycles during the Pennsylvanian to earliest Cisuralian in the Liujiang Coalfield from the North China Plate (NCP). We use integrated data from Zircon U-Pb dating, Hg/TOC ratios and $\delta^{13}C_{org}$ to recover temporal trends in volcanic intensity and relate these to fluctuations in the global carbon cycle and atmospheric pCO$_2$. Four new radiometric dates from tuffaceous claystones provide a precision stratigraphic framework and constrain the succession to ~322 to 301 Ma. Results date the Benxi Formation to the Bashkirian–Moscovian stages of the Carboniferous, and the Taiyuan Formation ranging from the Kasimovian stage of the Carboniferous to the Asselian stage of the Permian. Results from Hg/TOC ratios record four peaks of volcanic intensity from the Bashkirian to the Carboniferous-Permian (C-P) transition period, and two low ebbs during the early-middle Bashkirian and the early-middle Moscovian. Peaks in volcanic intensity coincide with the four negative excursions of $\delta^{13}C_{org}$ and correlate with volcanism in the North China Plate and NW Europe, inferring volcanic drivers for the carbon isotope excursions and perturbations in the global carbon cycle. Periods of higher atmospheric pCO$_2$ correlate to interglacial intervals, the two lower ebbs in pCO$_2$ correlate with two positive isotope plateaus, while periods of lower atmospheric pCO$_2$ and cooling correlate with glacial intervals C3 and C4 recognized from other sections globally. Results suggest volcanism to be a significant driver for late Pennsylvanian to earliest Cisuralian shifts in global climates from glacial to interglacial through greenhouse gas emissions and changes to the global carbon cycle. Our results represent an important contribution to the development of an accurate chronostratigraphy for the continental facies of the NCP during the Pennsylvanian and earliest Permian, enabling correlation of volcanic and climate events including glacial and interglacial cycles.

1. Introduction

The late Paleozoic ice age (LPIA; ca. 360–260 Ma) during the Carboniferous and Permian included multiple shifts between glacial and interglacial conditions that correspond to the waxing and waning of ice-sheets in high-latitude Gondwana (e.g., Isbell et al., 2003; Fielding et al., 2008). It represents vegetated Earth's only known transition from icehouse-to-greenhouse conditions (Montañez et al., 2007), with direct

relevance to potential future anthropogenic climate change. The onset, development and demise of these climate shifts has been linked to variations in coal forests dynamics (Cleal and Thomas, 2005), atmospheric partial pressure of CO$_2$ (pCO$_2$) (Montañez et al., 2007, 2016; Richey et al., 2020), tectonically paced rock weathering regimes (Goddéris et al., 2017) and volcanism (Yin et al., 2007). Uplift from the Hercynian Orogeny during the Pennsylvanian led to increased chemical weathering and was sufficient to cause atmospheric CO$_2$ concentrations to fall,

triggering cooling (Goddéris et al., 2017). Similarly, expansion of peat-forming forests coincides with decreasing pCO$_2$ and global cooling, while their contraction coincides with increasing pCO$_2$ and global warming (Cleal and Thomas, 2005; Richey et al., 2020). However, the contribution of volcanism to the climate changes is controversial, because it can discharge large volumes of CO$_2$ and CH$_4$ into the atmosphere, elevating atmospheric greenhouse gas concentration and causing global warming (Yin et al., 2007; Bond and Grasby, 2017), but can also lead to global cooling through negative radiative forcing of volcanic- sourced sulfate aerosols (Soreghan et al., 2019).

Hg concentrations have been used as a proxy for ancient volcanism because volcanic eruptions can release significant amounts of Hg to the Earth-surface system (Pyle and Mather, 2003; Grasby et al., 2013; Percival et al., 2017). In the atmosphere and oceans, Hg has a limited residence time before it is deposited on the Earth's surface (Shen et al., 2019b). As such, volcanic mercury release has the potential to produce a stratigraphic record of volcanism in contemporaneous sedimentary rocks. Carbon isotopic values (δ^{13}C$_{org}$) in land plant residues have been used to reconstruct the carbon isotope composition of atmospheric CO$_2$, which mirrors changes in global carbon cycling (e.g., Faure et al., 1995). δ^{13}C$_{org}$ values in sediments is another proxy for ancient volcanic activity, the coincidence of Hg enrichment and carbon isotope negative excursions implies a common source in heating of organic-rich sediments by magma intrusion probably at the onset of sill-intrusion in Large Igneous Provinces (LIPs) (Shen et al., 2019b).

In the present study, we investigate the continental strata from the Pennsylvanian to early Cisuralian Benxi and Taiyuan formations to investigate the relationships between volcanism, climate, and environment. Focusing on the Shimenzhai profile in the Liujiang coalfield in the northeastern part of the North China Plate, we analyze mercury concentrations to identify intervals of volcanism and δ^{13}C$_{org}$ values to evaluate perturbations in the global carbon cycle. Using four new zircon U-Pb dates determined from interbedded tuffaceous claystone horizons, we provide a revised stratigraphic framework for the Benxi and Taiyuan formations including assessments of depositional rates between the dated horizons. The new radiometric dates also offer the potential to correlate individual tuff horizons across the NCP and determine their spatial extents.

2. Geological background

During the Pennsylvanian, the NCP, surrounded by the Inner Mongolia uplift (IMU) to the north and the North Qinling Belt (NQB, or Funiu Paleo-land) to the south, was located in the northeastern margin of the Paleo-Tethys Ocean (PTO) (Fig. 1a), with a latitude of approximately 10–20°N (Shang, 1997; Blakey, 2011; Dong and Santosh, 2016). It was separated from the South China Plate by the PTO and the Mongolian Plate by the Paleo-Asian Ocean (PAO) (Fig. 1a). Southward subduction of oceanic crust from the PAO beneath the NCP (Fig. 1b; Shang, 1997; Zhang et al., 2014), beginning in the mid-Carboniferous (c.
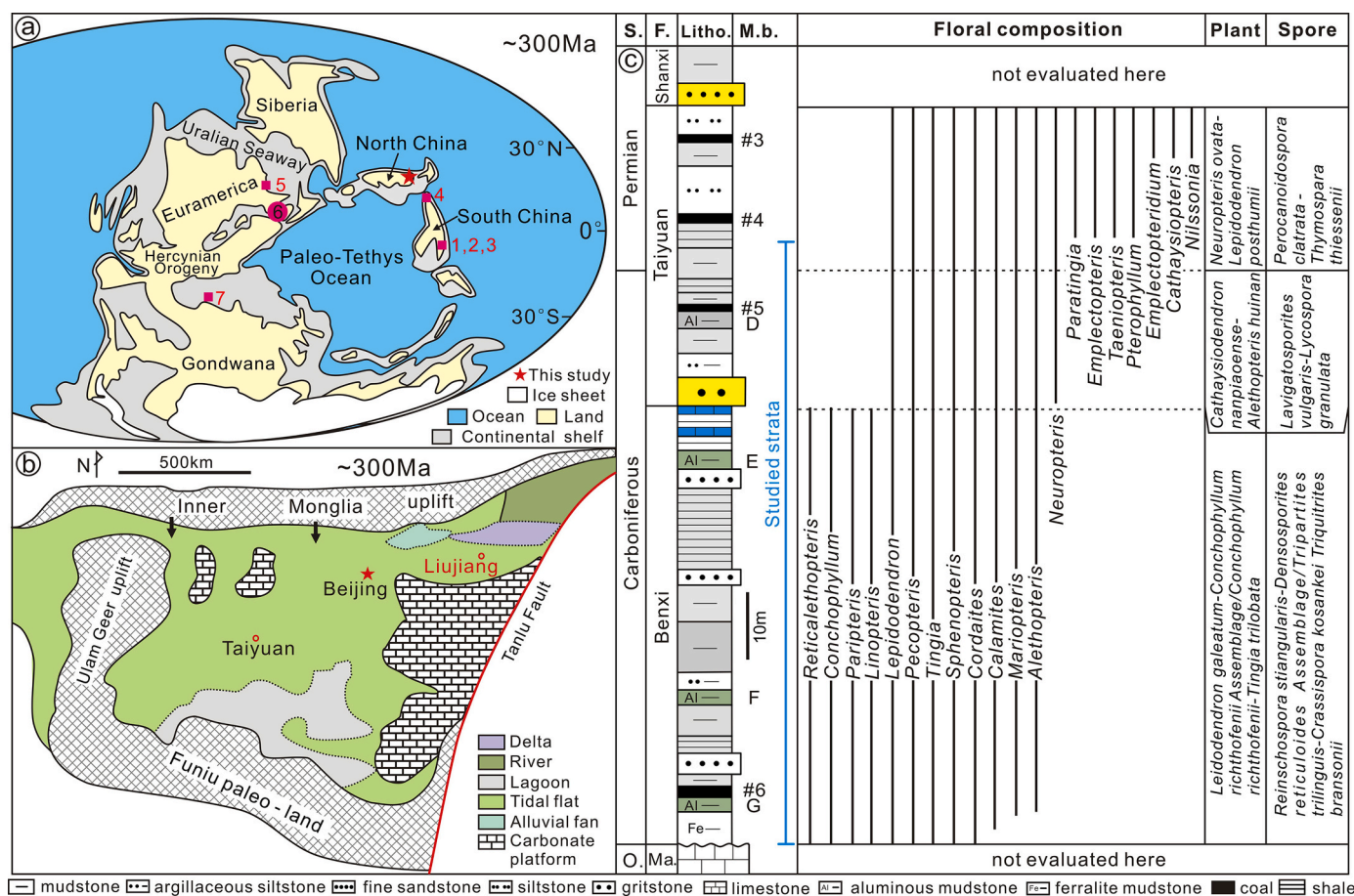
Fig. 1. Location and geological context for the research area. a, Paleogeographic reconstruction for the Pennsylvanian (~300 Ma) showing location of North China Plate (modified from Blakey, 2011). Also shown are the positions of the Youjiang (1), Naqing (2) and Zhongdi (3) profiles in South China, and the Kongshan (4) profile in East China. Locations of the Skagerrak-Centered Large Igneous Province (SCLIP; 6) and the south west Africa (7) volcanic activity in Namibia are indicated. b, Map of the North China Plate showing the location of study area and the sedimentary environment during deposition of the late Benxi Formation (~300 Ma; modified from Shang, 1997); black arrow represents the direction of source. c, Floral composition and the plant megafossil and, sporomorph assemblages from Wang (2010). Abbreviations: S. - Stage; F. - Formation; Litho. - lithofacies; M. b. - Marked bed; Plant a. - Plant assemblage; Spore a. - Spore assemblage; O. - Ordovician; Ma. - Majaigou. Note: position of the C-P boundary is from previous biostratigraphic syntheses (Wang, 2010).

330 Ma), resulted in episodic volcanism across much of the IMU (Zhang et al., 2009). However, the environmental and climatic effects of this volcanism on the continental settings in the NCP are largely unknown.

The stratigraphic succession, rock types, fossils and marker beds in the target strata in the Liujiang coalfield are shown in Fig. 1c. These unconformably overlie Ordovician limestones, and comprise the continuous Benxi Formation and lower part of overlying Taiyuan Formation (Shang, 1997). The Benxi Formation was deposited in tidal flat and lagoon settings and mainly comprises dark-gray mudstones with lenticular sandstones and thin coal seams. The Taiyuan Formation is separated from the Benxi Formation by a layer of gray, thick-bedded coarse-grained quartz sandstone, with the remainder of the Taiyuan Formation comprising mudrocks, limestones and sandstones deposited in a range of carbonate and detrital costal depositional environments. Four gray-white claystone beds (named G, F, E, and D in ascending order; see Fig. 1) occur in the succession that are each homogenous and powdery in the field, lack bedding features and fossils, and contain a large number of well-sorted, euhedral, zoned zircon crystals (especially for the #G claystone) of volcanic origin. The claystone beds are interpreted to have originated as air-fall tuffs (Yang et al., 2020) but appear to have deposited in still water conditions alongside other clay minerals. As a result, they are termed tuffaceous claystones here.

Based on the composition of fossil plant and sporopollen assemblages, the base of the Benxi and Taiyuan formations have been dated to the early Bashkirian and the early to middle Moscovian respectively, and the C-P boundary was placed near the middle of the Taiyuan Formation (Wang, 2010). However, in the Paleozoic, fossil plant and sporopollen biostratigraphy in terrestrial settings typically provide comparatively coarse stratigraphic resolution in contrast to more precise methods including radiometric dating. In the NCP, except for tuffaceous claystone layer #G, the other three layers have previously not been dated by radiometric methods (Liu et al., 2014).

3. Materials and analytical methods

From the Shimenzhai profile (40.0920°N, 119.5850°E) in the Liujiang coalfield, fresh mudstone (47 samples) were collected from the Benxi Formation to the lower member of Taiyuan Formation. Sampling locations are shown in Fig. 2. Each mudstone sample was crushed below 200 mesh and divided into three parts for (1) mercury concentration analysis, (2) total organic carbon (TOC) analysis, (3) $\delta^{13}C_{org}$ analysis, (4) major elements analysis and (5) total sulfur analysis. Mercury concentrations were measured at the State Key Laboratory of Coal Resources and Safe Mining (Beijing), total organic carbon (TOC), $\delta^{13}C_{org}$, major
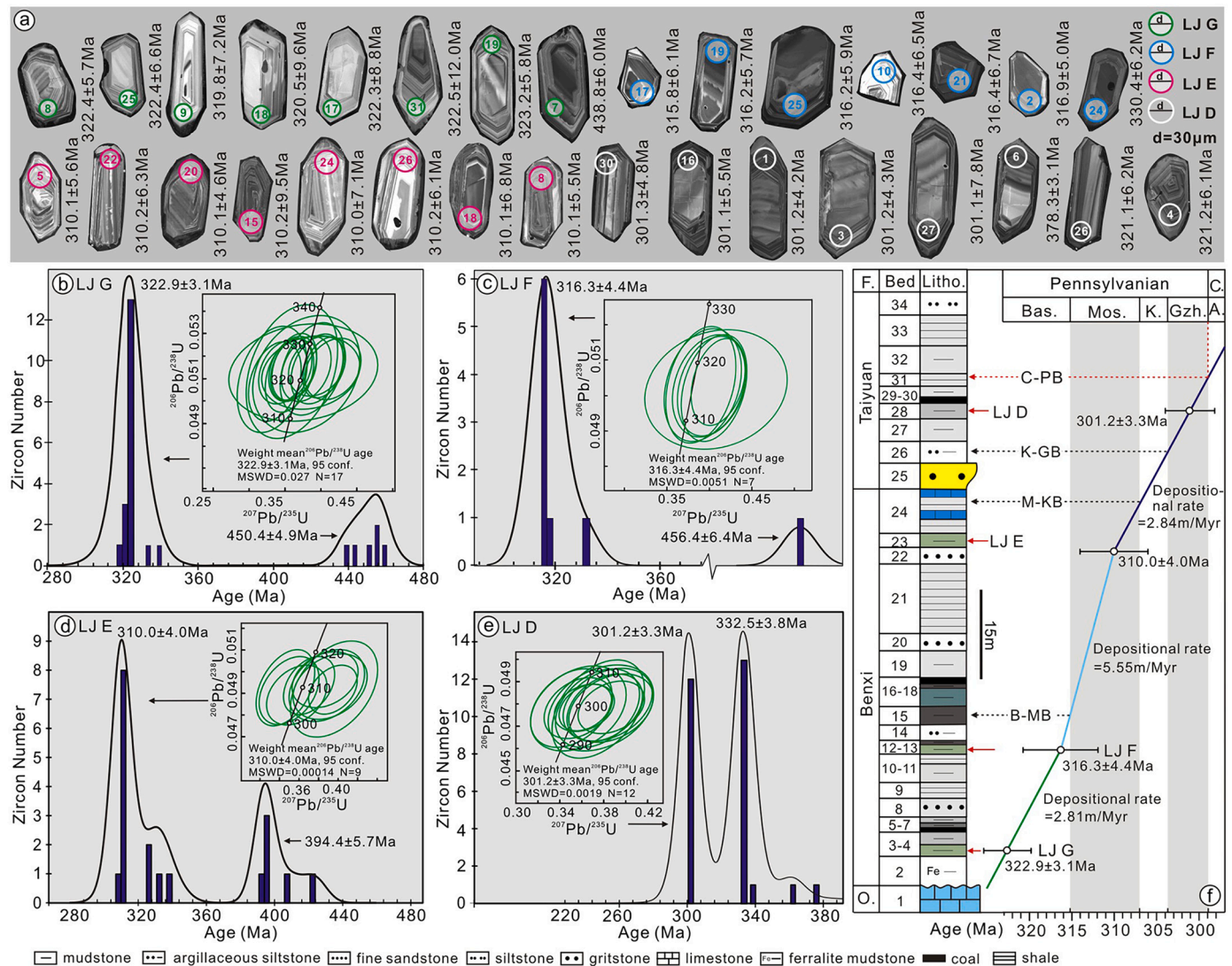
Fig. 2. Zircon $^{206}Pb/^{238}U$ age distribution diagrams. a, Example zircon crystals from each sample. b, Sample LJ #G. c, Sample LJ #F. d, Sample LJ #E, e, Sample LJ #D. f, Age model through the Shimenzhai profile succession. Abbreviations: F. - Formation, O. - Ordovician, Litho. -lithofacies, P. - Permian, Bas. - Bashkirian, Mos. - Moscovian, K. - Kasimovian, Gzh. - Gzhelian, A. – Asselian. Note: position of C-P boundary is from the precision dating developed in this paper.

elements and total sulfur (TS) were measured at the Beijing Research Institute of Uranium Geology. Mercury concentration analysis was undertaken using a mercury analyzer (Lumex RA-915+) with lower detection limits of 2 ng/g and the relative analysis error of ±5%. Samples for TOC were first treated with phosphoric acid to remove inorganic carbon, and then the TOC values were measured using a carbon-sulfur analyzer (CS580-A) with the lower detection limits of 100 mg/g and the absolute analysis error of ±0.2%. $\delta^{13}C_{org}$ analysis was performed using a stable isotope mass spectrometer (MAT253), and $\delta^{13}C_{org}$ values are expressed in per mil (‰) with respect to the Vienna Pee Dee Belemnite (VPDB) standard, with the absolute analysis error of ±0.1‰. Major elements analysis was undertaken with an X-ray fluorescence spectrometer (PW2404) with the relative analysis error of ±5%. Total sulfur analysis was performed using a carbon-sulfur analyzer (Eltra CS580-A) with the lower detection limits of 30 ppm and the absolute analysis error of ±5%. More details of the analytical method are described by Liao et al. (2016), Hu et al. (2020) and Chu et al. (2020). In this study, mercury enrichment anomalies have been used to indicate the presence of volcanic activity due to its relationship with volcanic eruptions and magmatic intrusions (Grasby et al., 2013; Chen and Xu, 2019; Wang et al., 2019).

Samples for zircon $^{206}Pb/^{238}U$ dating were collected from tuffaceous claystone beds G, F, E and D (Figs. 1c and 3) and named LJ G, LJ F, LJ E and LJ D respectively. After crushing, grinding, sieving and heavy liquid and magnetic separation, euhedral zircon crystals with clear oscillatory zoning under the cathodoluminescence (CL) microscope were selected for U-Pb zircon isotope analysis. U-Pb dating was conducted at the State Key Laboratory Geological Processes and Mineral Resources (Beijing), using a Thermo Fisher's X-Series 2 ICP-MS instrument to acquire ion-signal intensities. Laser sampling was performed using a Coherent's GeoLasPro-193 nm system. Zircon 91,500 and Plešovice zircon were used as an external standard for U-Th-Pb isotopic ratios and monitoring the standard of each analysis (Wiedenbeck et al., 1995, 2004; Sláma et al., 2008) respectively. Data Cal and Isoplot 3.0 software were used for the age analysis, calculation, and the drawing of concordia diagrams from the ICPMS data.

4. Results and analysis

4.1. U-Pb zircon dating

The particle size of zircons from the tuffaceous claystone beds varies from 50 to 200 μm. Individual zircon crystals show euhedral morphology and clear oscillatory zoning in cathodoluminescence (CL) distinctive of magmatic zircon (Fig. 2a). $^{206}Pb/^{238}U$ dating results for the four samples are shown in Fig. 2 and Table 1.

From sample LJ G a total of 25 concordant age values were determined with a bimodal age distribution (Fig. 2b); the younger peak has a weighted mean $^{206}Pb/^{238}U$ age of 322.9 ± 3.1 Ma (MSWD = 0.027, N = 17), while the older peak has a weighted mean $^{206}Pb/^{238}U$ age of 450.4 ± 4.9 Ma (MSWD =1.7, N = 6). Sample LJ F yielded 8 concordant age values distributed in a single peak (Fig. 2c), with a weighted mean $^{206}Pb/^{238}U$ age of 316.3 ± 4.4 Ma (MSWD = 0.0051, N = 7). Sample LJ E yielded 19 concordant age values with a bimodal distribution (Fig. 2d); the younger peak has a weighted mean $^{206}Pb/^{238}U$ age of 310.0 ± 4.0 Ma (MSWD = 0.00014, N = 9), while the older peak has a weighted mean $^{206}Pb/^{238}U$ age of 394.4 ± 5.7 Ma (MSWD = 0.097, N = 4). Sample LJ D, the stratigraphically youngest, yielded 28 concordant age values with a bimodal distribution (Fig. 2e); the younger peak has a weighted mean $^{206}Pb/^{238}U$ age of 301.2 ± 3.3 Ma (MSWD = 0.0019, N = 12) while the older peak has a weighted mean $^{206}Pb/^{238}U$ age of 332.5 ± 3.8 Ma (MSWD = 0.0036, N = 14).

We interpret the weighted mean ages from the younger peaks as the sedimentary ages of the tuffaceous claystone horizons for the following reasons. Firstly, the Th/U ratios of the zircon crystals vary from 0.41–2.70 ($\bar{x}$ = 0.96, Table 1) and have euhedral crystal morphologies with clear oscillatory zoning that are indicative of volcanism-sourced zircons. Secondly, during the Pennsylvanian frequent volcanic activity in IMU source area provides the possibility for the frequent inputs of tuffaceous and pyroclastic materials into the depositional basin, and the ages of the younger peaks are consistent with a Pennsylvanian age (Fig. 2f). Finally, the distribution of the four younger peak weighted mean ages is consistent with the Pennsylvanian ages determined from biostratigraphy and regional lithostratigraphy, unlike the older peaks that provide ages that are consistently older than the Pennsylvanian.
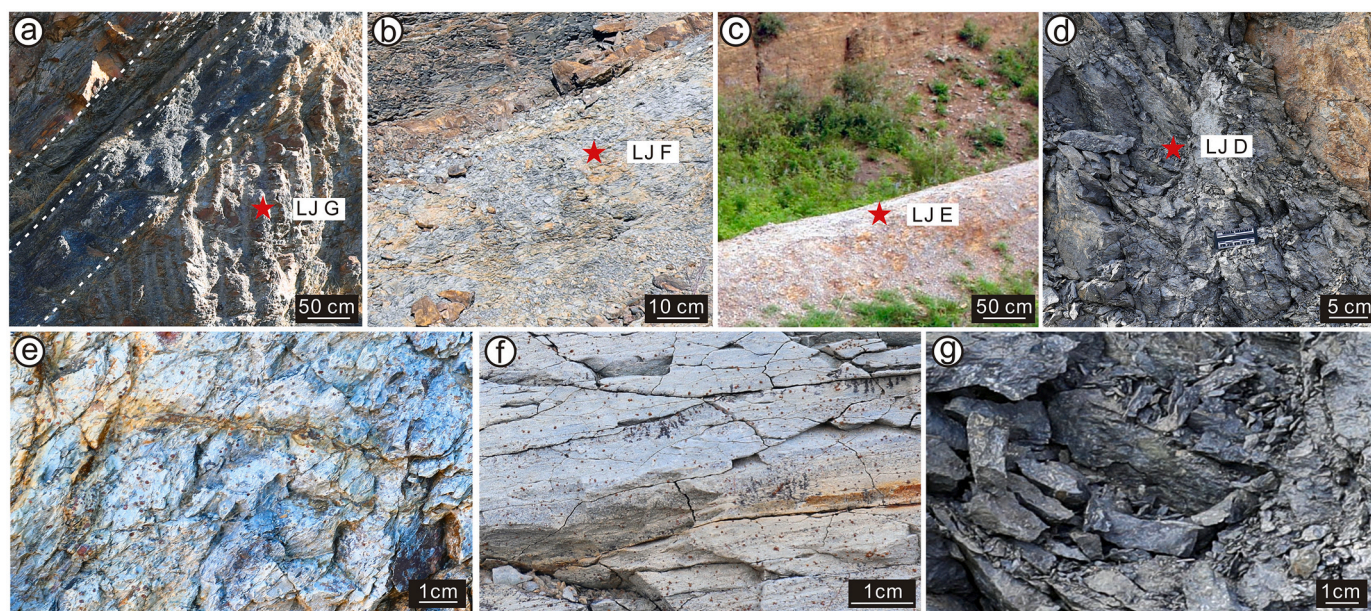
Fig. 3. a–d, Field photographs showing the locations of tuffaceous claystone samples for radiometric dating in the Shimenzhai profile. a, G and sample LJ G. b, F and sample LJ F. c, E sample LJ E. d, D and sample LJ D. e, Enlargement from a showing detail of LJ G. f, Enlargement from b showing detail of LJ F. g, Enlargement from d showing detail of LJ D. The red five-pointed stars represent the location of the samples. (For interpretation of the references to colour in this figure legend, the reader is referred to the web version of this article.)

Table 1
Zircon U-pb isotope results for the tuffite of LJ D, LJ E, LJ F, and LJ G.

Sample number	Zircon sample number	Content (µg/g)		Th/U	Isotope ratios				rho	Age		Concordance
		Th	U	U	$^{207}Pb/^{235}U$	$^{207}Pb/^{235}U$	$^{206}Pb/^{238}U$	$^{206}Pb/^{238}U$		$^{206}Pb/^{238}U$	$^{206}Pb/^{238}U$	
		232	238		Ratio	1sigma	Ratio	1sigma		Age (Ma)	1sigma	
LJD	LJD-29	486.4	653.5	0.74	0.0039	0.3751	0.0278	0.0478	0.0015	300.8	9.0	92%
	LJD-12	219.3	212.1	1.03	0.0044	0.3568	0.0288	0.0478	0.0013	301.0	7.7	97%
	LJD-25	226.5	486.7	0.47	0.0038	0.3743	0.0253	0.0478	0.0012	301.1	7.2	93%
	LJD-26	341.5	424.1	0.81	0.0040	0.3866	0.0254	0.0478	0.0010	301.1	6.2	90%
	LJD-16	412.4	519.3	0.79	0.0032	0.3569	0.0206	0.0478	0.0009	301.1	5.5	97%
	LJD-27	316.1	431.0	0.73	0.0037	0.3504	0.0245	0.0478	0.0012	301.1	7.2	98%
	LJD-10	146.8	167.8	0.88	0.0056	0.3773	0.0317	0.0478	0.0013	301.1	7.8	92%
	LJD-3	436.9	525.1	0.83	0.0026	0.3623	0.0181	0.0478	0.0007	301.2	4.3	95%
	LJD-4	268.2	474.4	0.57	0.0039	0.3809	0.0227	0.0478	0.0010	301.2	6.1	91%
	LJD-1	312.2	604.8	0.52	0.0023	0.3632	0.0158	0.0478	0.0007	301.2	4.2	95%
	LJD-30	347.4	448.3	0.77	0.0029	0.3869	0.0200	0.0478	0.0008	301.3	4.8	90%
	LJD-13	710.0	531.5	1.34	0.0037	0.3836	0.0268	0.0480	0.0011	302.0	6.6	91%
	LJD-11	270.2	388.8	0.69	0.0034	0.4248	0.0233	0.0529	0.0009	332.0	5.7	92%
	LJD-2	223.0	308.8	0.72	0.0070	0.4054	0.0460	0.0529	0.0016	332.1	9.8	96%
	LJD-7	363.9	316.9	1.15	0.0035	0.4241	0.0272	0.0529	0.0010	332.1	6.4	92%
	LJD-18	460.8	273.5	1.69	0.0038	0.4098	0.0273	0.0529	0.0009	332.1	5.4	95%
	LJD-21	1469.7	544.1	2.70	0.0030	0.3717	0.0195	0.0529	0.0010	332.2	6.1	96%
	LJD-20	548.7	459.2	1.19	0.0024	0.4043	0.0163	0.0529	0.0007	332.5	4.5	96%
	LJD-28	783.4	467.8	1.67	0.0061	0.4273	0.0473	0.0529	0.0016	332.6	9.8	91%
	LJD-23	302.5	356.1	0.85	0.0045	0.4245	0.0307	0.0530	0.0013	332.9	8.1	92%
	LJD-24	274.9	330.7	0.83	0.0033	0.4170	0.0214	0.0530	0.0009	332.9	5.6	93%
	LJD-8	161.7	178.0	0.91	0.0087	0.4341	0.0601	0.0530	0.0019	333.1	11.4	90%
	LJD-15	440.3	256.2	1.72	0.0047	0.4293	0.0323	0.0530	0.0012	333.1	7.2	91%
	LJD-22	574.7	514.8	1.12	0.0033	0.4337	0.0231	0.0532	0.0009	334.3	5.7	91%
	LJD-31	96.2	116.6	0.83	0.0096	0.4203	0.0517	0.0536	0.0061	336.5	7.1	94%
	LJD-19	834.5	515.9	1.62	0.0042	0.3971	0.0309	0.0538	0.0009	337.7	5.6	99%
	LJD-9	261.8	182.3	1.44	0.0053	0.4753	0.0369	0.0577	0.0012	361.6	7.5	91%
	LJD-6	1206.6	566.7	2.13	0.0118	0.4979	0.0797	0.0604	0.0064	378.3	3.1	91%
LJ E	LJE-24	505.3	354.5	1.43	0.3461	0.0197	0.0493	0.0012	0.4141	310.0	7.1	97%
	LJE −20	295.6	542.5	0.54	0.3936	0.0165	0.0493	0.0007	0.3628	310.1	4.6	91%
	LJE −5	231.4	268.1	0.86	0.3627	0.0206	0.0493	0.0009	0.3272	310.1	5.6	98%
	LJE −9	278.7	207.5	1.34	0.3787	0.0242	0.0493	0.0009	0.3004	310.1	5.8	94%
	LJE-8	249.3	608.5	0.41	0.3788	0.0175	0.0493	0.0009	0.3932	310.1	5.5	94%
	LJE −18	365.0	729.3	0.50	0.3854	0.0253	0.0493	0.0011	0.3404	310.1	6.8	93%
	LJE −22	402.6	340.3	1.18	0.3512	0.0198	0.0493	0.0010	0.3658	310.2	6.3	98%
	LJE −15	525.3	544.6	0.96	0.3945	0.0307	0.0493	0.0015	0.4038	310.2	9.5	91%
	LJE −26	281.2	168.2	1.67	0.3917	0.0251	0.0493	0.0010	0.3170	310.2	6.1	92%
	LJE −10	341.5	215.8	1.58	0.3867	0.0217	0.0518	0.0011	0.3945	325.6	7.0	98%
	LJE −16	524.5	273.8	1.92	0.4236	0.0341	0.0522	0.0021	0.4944	328.0	12.7	91%
	LJE −1	81.9	136.3	0.60	0.4193	0.0327	0.0530	0.0010	0.2500	332.9	6.3	93%
	LJE −25	437.5	284.4	1.54	0.4391	0.0460	0.0538	0.0014	0.2475	337.7	8.5	90%
	LJE −7	284.3	280.0	1.02	0.4617	0.0237	0.0626	0.0010	0.3231	391.5	6.3	98%
	LJE −27	445.7	374.7	1.19	0.5002	0.0258	0.0631	0.0009	0.2802	394.2	5.5	95%
	LJE −2	365.6	349.9	1.04	0.4890	0.0203	0.0632	0.0009	0.3364	394.9	5.4	97%
	LJE −4	370.8	356.7	1.04	0.5146	0.0268	0.0634	0.0010	0.3093	396.1	6.2	93%
	LJE −6	212.6	232.7	0.91	0.5147	0.0275	0.0654	0.0012	0.3345	408.5	7.1	96%
	LJE −21	336.5	304.3	1.11	0.5011	0.0239	0.0679	0.0012	0.3598	423.4	7.0	97%
LJ F	LJF-21	179.1	227.0	0.79	0.3461	0.0197	0.0493	0.0012	0.4141	316.4	6.7	94%
	LJF-14	235.3	298.0	0.79	0.3936	0.0165	0.0493	0.0007	0.3628	315.6	6.9	90%
	LJF-17	279.7	209.2	1.34	0.3627	0.0206	0.0493	0.0009	0.3272	315.8	6.1	90%
	LJF-19	278.2	267.4	1.04	0.3787	0.0242	0.0493	0.0009	0.3004	316.2	5.7	91%
	LJF-25	358.2	428.0	0.84	0.3788	0.0175	0.0493	0.0009	0.3932	316.2	5.9	92%
	LJF-10	136.6	185.6	0.74	0.3854	0.0253	0.0493	0.0011	0.3404	316.4	6.5	93%
	LJF-2	210.5	257.2	0.82	0.3512	0.0198	0.0493	0.0010	0.3658	316.9	5.0	90%
	LJF-24	249.9	322.1	0.78	0.3945	0.0307	0.0493	0.0015	0.4038	330.4	6.2	90%
	LJF-5	153.9	331.2	0.46	0.3917	0.0251	0.0493	0.0010	0.3170	456.4	6.4	99%
LJ G	LJG-9	146.8	127.4	1.15	0.3360	0.0242	0.0509	0.0012	0.3183	319.8	7.2	91%
	LJG-18	75.4	87.1	0.87	0.3323	0.0322	0.0510	0.0016	0.3150	320.5	9.6	90%
	LJG-30	267.1	301.3	0.89	0.3566	0.0222	0.0512	0.0011	0.3408	321.6	6.6	96%
	LJG-29	88.8	98.6	0.90	0.3801	0.0493	0.0512	0.0017	0.2576	321.9	10.5	98%
	LJG-17	74.7	106.0	0.70	0.3757	0.0684	0.0513	0.0014	0.1531	322.3	8.8	99%
	LJG-8	176.4	196.6	0.90	0.3476	0.0222	0.0513	0.0009	0.2823	322.4	5.7	93%
	LJG-25	91.8	108.3	0.85	0.3862	0.0453	0.0513	0.0011	0.1788	322.4	6.6	97%
	LJG-31	250.7	238.0	1.05	0.3599	0.0420	0.0513	0.0020	0.3271	322.5	12.0	96%
	LJG-26	111.3	261.2	0.43	0.3592	0.0192	0.0514	0.0009	0.3276	323.1	5.5	96%
	LJG-19	179.3	194.4	0.92	0.3799	0.0229	0.0514	0.0010	0.3067	323.2	5.8	98%
	LJG-27	123.4	143.2	0.86	0.3884	0.0294	0.0514	0.0014	0.3481	323.2	8.3	96%
	LJG-21	105.5	143.5	0.74	0.3950	0.0241	0.0514	0.0010	0.3262	323.3	6.3	95%
	LJG-12	128.6	189.7	0.68	0.4173	0.0257	0.0514	0.0009	0.2825	323.3	5.5	90%
	LJG-4	185.6	190.6	0.97	0.3610	0.0219	0.0514	0.0010	0.3052	323.3	5.8	96%
	LJG-15	248.5	455.9	0.54	0.4048	0.0195	0.0515	0.0009	0.3583	323.7	5.5	93%

Table 1 (*continued*)

Sample number	Zircon sample number	Content (µg/g) Th	Content (µg/g) U	Th/ U	Isotope ratios $^{207}Pb/^{235}U$ Ratio	$^{207}Pb/^{235}U$ 1sigma	$^{206}Pb/^{238}U$ Ratio	$^{206}Pb/^{238}U$ 1sigma	rho	Age $^{206}Pb/^{238}U$ Age (Ma)	$^{206}Pb/^{238}U$ 1sigma	Concordance
		232	238									
	LJG-22	155.9	252.8	0.62	0.3631	0.0205	0.0515	0.0010	0.3349	323.8	6.0	97%
	LJG-28	151.5	236.8	0.64	0.3951	0.0259	0.0515	0.0009	0.2577	324.0	5.3	95%
	LJG-13	165.3	161.5	1.02	0.3516	0.0236	0.0530	0.0008	0.2379	333.0	5.2	91%
	LJG-11	55.0	94.8	0.58	0.3970	0.0256	0.0539	0.0012	0.3380	338.1	7.2	99%
	LJG-7	152.6	219.6	0.69	0.5503	0.0300	0.0704	0.0010	0.2598	438.8	6.0	98%
	LJG-2	194.5	374.2	0.52	0.5416	0.0216	0.0712	0.0010	0.3506	443.2	6.0	99%
	LJG-1	183.1	375.2	0.49	0.5338	0.0217	0.0725	0.0009	0.3027	451.1	5.4	96%
	LJG-10	139.7	177.5	0.79	0.6158	0.0337	0.0733	0.0013	0.3131	455.8	7.5	93%
	LJG-3	176.5	356.6	0.49	0.5823	0.0233	0.0733	0.0009	0.3028	455.8	5.3	97%
	LJG-14	167.8	313.1	0.54	0.5687	0.0216	0.0738	0.0010	0.3689	459.0	6.2	99%

Using the $^{206}Pb/^{238}U$ zircon ages an age model for the sedimentary succession can be generated. From the Benxi Formation, tuffaceous claystone LJ G from Bed 3 is dated to 322.9 ± 3.1 Ma during the earliest Bashkirian, sample LJ F from Bed 12 to 316.3 ± 4.4 Ma during the late Bashkirian, while sample LJ E from Bed 23 in the upper part of the Benxi Formation is dated to 310.0 ± 4.0 Ma during the late Moscovian (Fig. 2f). Sample LJ D from Bed 28 in the lower part of the Taiyuan Formation is dated to 301.2 ± 3.3 Ma during the late Ghzelian. Using linear interpolation and without differential compaction correction, approximate average rates of deposition have been determined from the chronostratigraphic framework between the four radiometric ages (Fig. 2f). Between LJ G and LJ F the average depositional rate is 2.81 m/ Myr, and between LJ F and LJ E it increases to 5.55 m/Myr, while between LJ E and LJ D is reduces to 2.84 m/Myr (Fig. 2f). These allow us to assign the base of the Moscovian to Bed 15, the base of the Kasimovian to Bed 24, the base of the Gzhelian to Bed 26, and the base of the Asselian to Bed 31. These conclusions are broadly consistent with previous biostratigraphic estimates (Shang, 1997; Wang, 2010), and among them, our estimation of the Carboniferous-Permian boundary from the zircon dates is approximately consistent with the biostratigraphic analysis of Wang (2010).

4.2. TOC, mercury, aluminum (Al) and total sulfur (TS) values

Results for TOC, mercury, aluminum (Al) and total sulfur (TS) are shown in Table 2 and Fig. 4a–b, d–e. TOC values vary from 0.20%–1.30% (mean ($\bar{x}$) = 0.46%) (Fig. 4b). The lower TOC values are mainly distributed during the Bashkirian to Gzhelian stages of the Carboniferous, and the higher TOC values appear during the earliest Asselian stage of the Permian. The values of Al_2O_3 concentrations vary from 5.08%–33.30% ($\bar{x}$ = 19.73%) (Fig. 4e) and TS concentrations vary from 0.003%–0.115% ($\bar{x}$ = 0.020%) (Fig. 4f).

Hg concentrations vary from 2.24 ppb–177.00 ppb ($\bar{x}$ = 27.19 ppb) (Fig. 4a). In continental strata, Hg is usually hosted by organic matter, sulfide, and clay minerals (e.g., Grasby et al., 2013, 2019; Shen et al., 2019a, 2019b). In the study area, Hg concentration shows positive correlation with TOC (correlation coefficient (r) = +0.56 with 99% confidence level, number of samples (n) = 47) and total sulfide (r = +0.37 with 99% confidence level, *n* = 47) and have negative correlation with Al (*r* = −0.18, n = 47) (Fig. 5a–c). This may indicate that Hg is present in both sulfides and organic matter (e.g., Shen et al., 2020). However, all the TS content values in the study area are less than 1.0% and the TS/TOC ratios are less than 0.35, suggesting that organic matter is the main host of Hg according to the TOC-TS relationships (Fig. 5d) (e. g., Grasby et al., 2013, 2019; Wang et al., 2019; Shen et al., 2019a, 2020). Thus, Hg concentrations are normalized to total organic carbon (TOC) content to discern enrichments independent of variations in TOC. Hg/TOC ratios vary from 9.98 ppb/% to 198.88 ppb/% ($\bar{x}$ = 53.77 ppb/%) (Fig. 4c), and display four peaks here named VA-I, VA-II, VA-III, and VA-IV in ascending order and with peaks of 174.72 ppb/%, 129.41 ppb/%, 96.27 ppb/%, and 198.88 ppb/% respectively (Fig. 4c). The VA-

Table 2
Results of TOC, mercury (Hg), Hg/TOC ratios, alumina (Al_2O_3) and total sulfur (TS).

Sample number	$\delta^{13}C_{org}$ (‰)	TOC (%)	Hg (ppb)	Hg/TOC (ppb/%)	Al_2O_3 (%)	TS (%)
Sm32–2	−24.9	0.52	20.26	38.96	15.08	0.004
Sm32–1	−25.1	1.21	46.67	38.57	17.26	0.017
Sm31–2	−24.8	0.76	39.06	51.39	15.66	0.003
Sm31–1	−25.1	0.89	177.00	198.88	20.99	0.025
Sm30–2	−25.6	0.92	104.42	113.50	17.42	0.015
Sm30–1	−25.5	0.65	35.68	54.89	17.23	0.014
Sm29–2	−23.3	0.30	18.72	62.40	20.02	0.016
Sm29–1	−23.0	0.47	60.04	127.74	23.04	0.115
Sm27–4	−24.3	0.25	10.04	40.16	24.95	0.005
Sm27–3	−24.7	0.23	9.42	40.96	18.91	0.003
Sm27–2	−25.3	0.52	50.06	96.27	18.41	0.008
Sm26–1	−24.9	0.43	16.25	37.79	17.11	0.023
Sm23–4	−25.2	0.30	25.41	84.70	5.08	0.014
Sm23–1-2	−25.4	0.79	100.65	127.41	14.50	0.053
Sm23–1	−25.7	0.81	104.82	129.41	14.81	0.068
Sm23–1-1	−25.5	0.85	101.71	119.66	16.50	0.076
Sm22–3	−22.9	0.21	9.30	44.29	17.86	0.022
Sm22–2	−23.0	0.21	9.61	45.76	23.10	0.019
Sm22–1	−23.5	0.26	6.14	23.62	21.52	0.023
Sm20–3	−24.6	0.34	7.26	21.35	15.19	0.023
Sm20–2	−24.8	0.35	3.83	10.94	14.64	0.008
Sm20–1	−23.7	0.40	5.40	13.50	16.30	0.020
Sm18–4	−24.5	0.35	7.99	22.83	16.49	0.011
Sm18–3	−24.2	0.41	4.09	9.98	21.18	0.009
Sm18–2	−23.3	0.30	4.47	14.90	20.70	0.031
Sm17–1	−23.1	0.24	3.54	14.75	23.47	0.011
Sm16–2	−22.3	0.22	2.24	10.18	20.95	0.005
Sm16–1	−23.8	0.22	2.54	11.55	19.09	0.011
Sm15–2	−26.0	0.61	106.58	174.72	17.72	0.012
Sm15–1	−26.4	0.56	64.99	116.05	21.28	0.007
Sm14–1	−24.9	0.27	35.44	131.26	11.96	0.003
Sm13–1	−24.4	0.20	7.85	39.25	30.33	0.003
Sm12–2	−23.4	0.31	40.07	129.26	32.23	0.023
Sm12–1	−24.2	0.20	4.11	20.55	17.25	0.026
Sm11–2	−25.2	0.46	44.59	96.93	18.40	0.003
Sm11–1	−25.7	0.66	26.97	40.86	19.83	0.003
Sm10–2	−24.9	0.21	16.48	78.48	19.36	0.003
Sm10–1	−23.1	0.20	9.58	47.90	16.89	0.003
Sm9–1	−23.7	0.56	8.19	14.63	17.66	0.031
Sm8–1	−24.4	0.43	10.96	25.49	10.82	0.018
Sm7–1	−23.7	1.30	19.92	15.32	23.27	0.025
Sm5–3	−24.0	1.26	14.26	11.32	23.46	0.053
Sm5–2	−23.6	0.25	3.07	12.28	17.87	0.011
Sm5–1	−23.5	0.23	7.62	33.13	24.41	0.009
Sm4–1	−23.0	0.27	5.01	18.56	33.30	0.028
Sm3–2	−24.0	0.28	6.34	22.64	30.96	0.018
Sm2–1	−23.5	0.23	7.32	31.83	33.13	0.003

I, VA-II, VA-III, and VA-IV episodes of Hg enrichment correspond to four negative carbon isotope excursions.

In the study area the four Hg/TOC peaks vary from 129.41 ppb/%–198.88 ppb/%, with an average of 149.82 ppb/%. In general, these Hg/
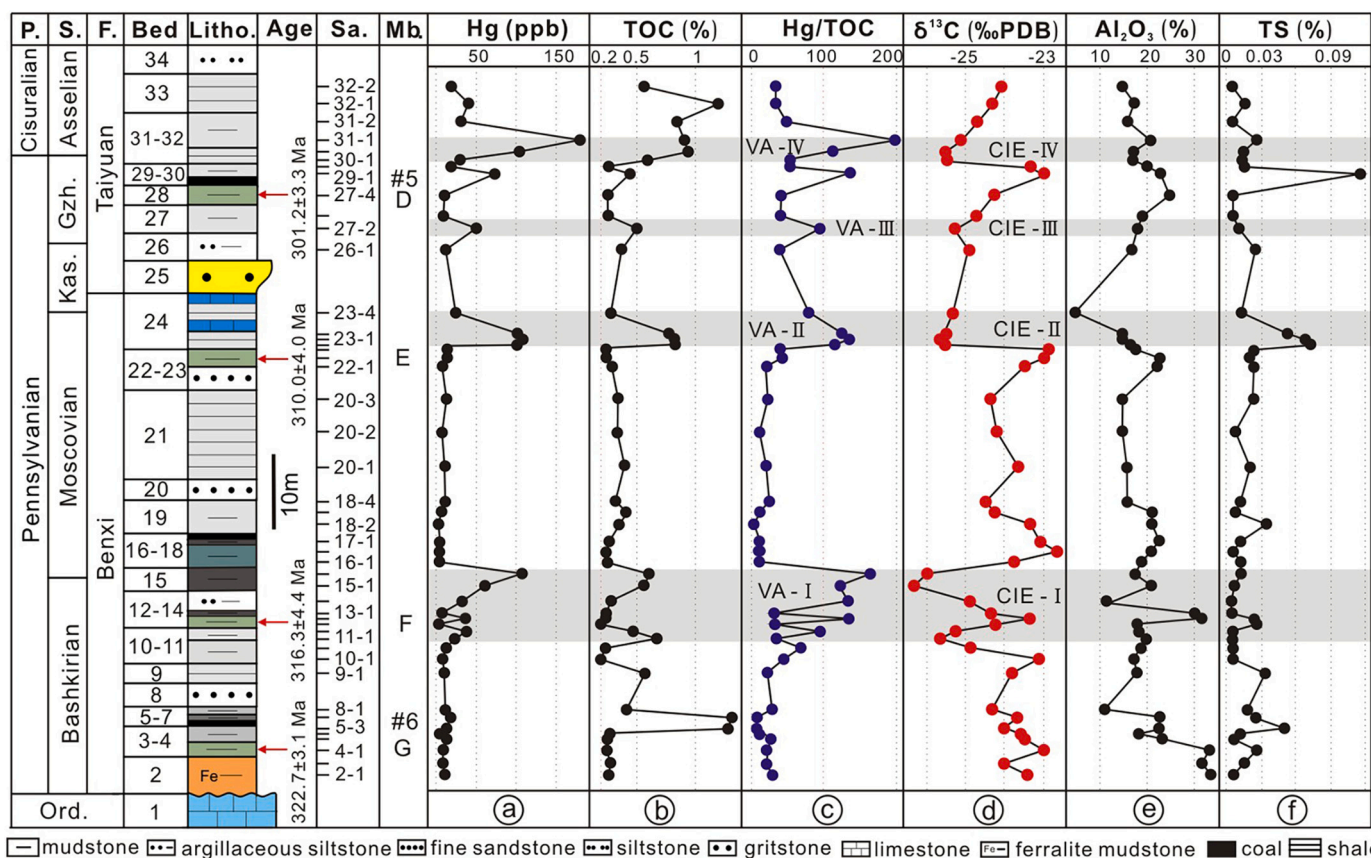
Fig. 4. Hg concentration, TOC values, Hg/TOC (ppb/%) ratios, δ¹³C_org values, Al₂O₃ concentrations and total sulfur (TS) concentrations from the Shimenzhai profile in the North China Platform. Abbreviations: P. - Period; S. - Stage; F. - formation; Ord. - Ordovician; Litho. - lithofacies; Sa. - sample; M.B.- marker bed;
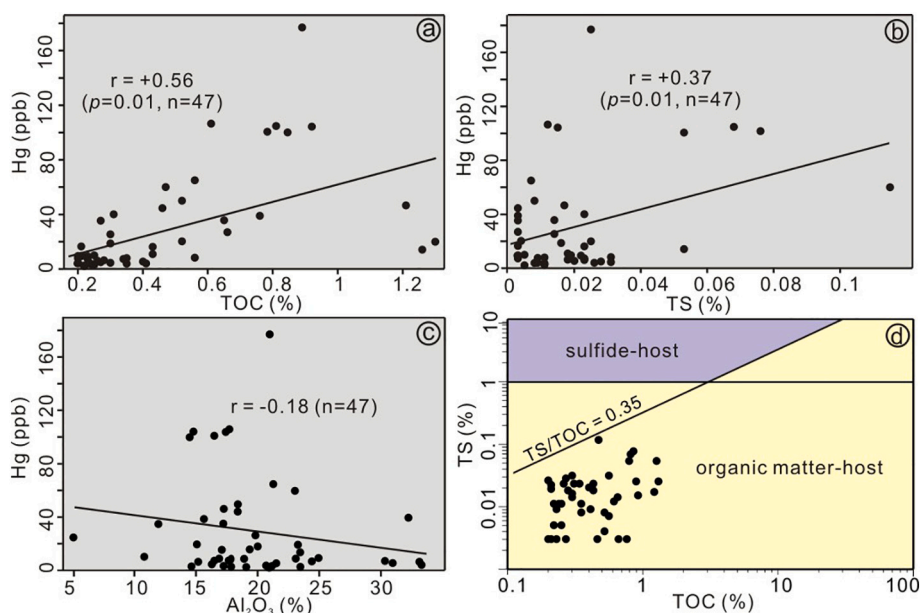

Fig. 5. Cross-plots of mercury (Hg) versus (a) total organic carbon (TOC) and (b) total sulfur (TS) and (c) aluminum (Al), and (d) TOC-TS. In (d) the thresholds of TS = 1.0% and TS/TOC = 0.35 separate most samples with a dominant organic Hg host (faint yellow field) from those with a dominant sulfide Hg host (purple field) (thresholds and base map from Shen et al., 2020). (For interpretation of the references to colour in this figure legend, the reader is referred to the web version of this article.)

TOC peak values are within the range of global data Hg/TOC values from volcanic events recorded from the Permian-Triassic and Triassic–Jurassic transition intervals where peak values are generally between approximately 100 ppb/%–800 ppb/% (e.g., Percival et al., 2017; Wang et al., 2019). We consider the mercury peak values in the study area to be reliable proxies for volcanism.

4.3. δ¹³C_org values

Results for δ¹³C_org are shown in Table 2 and Fig. 4d. δ¹³C_org values vary from −26.4‰ to −22.3‰ (x̄ = −24.3‰). In the Benxi Formation, there are two positive isotope plateaus, one during the early-middle Bashkirian and another during the early-middle Moscovian, separated

from each other by a negative carbon isotope excursion (CIE-I) during the late Bashkirian. CIE-I has two peaks of which the second corresponding to Beds 14–15 is largest. From the uppermost Benxi Formation (Bed 24) to the lower Taiyuan Foramtion (Bed 32), three negative carbon isotope excursions were recorded in the Moscovian to Asselian (CIE-II, CIE-III and CIE-IV). The four negative carbon isotope excursions of 3.8‰ (CIE-I), 3.4‰ (CIE- II), 0.4‰ (CIE-III), and 2.6‰ (CIE-IV) coincide with mercury peaks VA-I, VA-II, VA-III and VA-IV (Fig. 4c, d) from which volcanism is likely to be a causal mechanism for the perturbations in the carbon cycle.

5. Discussion

5.1. Stratigraphic correlation of sedimentary facies and volcanic events within North China Plate

The new radiometric ages provided here from the Benxi and Taiyuan formations represent an important step in developing a precise chronostratigraphic framework for the Pennsylvanian continental facies of the NCP, augmenting established bio- and lithostratigraphic approaches and the previously limited radiometric dates available (Liu et al., 2014; Schmidt et al., 2020; Yang et al., 2020). This is important because the

Benxi, Taiyuan and Shanxi formations are diachronous across the NCP (Shang, 1997; Peng et al., 2003), making precise correlation difficult.

In the northern source area (IMU) of the NCP, there are more than 20 records of volcanic events during the Pennsylvanian varying in age from ~298 to ~315 Ma. These are mainly intrusive rocks with lithologies including granodiorite and quartz diorite, gabbro, tonalite and granite (Zhang et al., 2009 and references therein). Modes of emplacement includes batholiths (e.g., the granodiorite batholith in Jianping with a surface area of about 500km^2 and the quartz diorite batholith in Daguangding with a surface area of about 200km^2), stocks (e.g., quartz diorite stocks in Boluonuo and Longhua with surface areas of about 80km^2 and 60 km^2 respectively), dikes and veins (Zhang et al., 2009 and references therein). In the sedimentary area of the NCP, twelve volcanic events in six phases were identified in the Benxi and Taiyuan formations by Zhong and Sun (1996) in the north, but these decrease southerly with increasing distance from the arc island to the north. These events offer great potential for future high precision stratigraphic correlation across the NCP and to determine the extent and timing of individual events.

From the Wuda Coalfield in Inner Mongolia (Fig. 6), a 66 cm thick air-fall tuff occurs betweeen coal seams #6 and #7 in the lower part of the Taiyuan Formation and preserves an in-situ peat forming forest community (Wang et al., 2012; Wang et al., 2019). After tuff deposition,
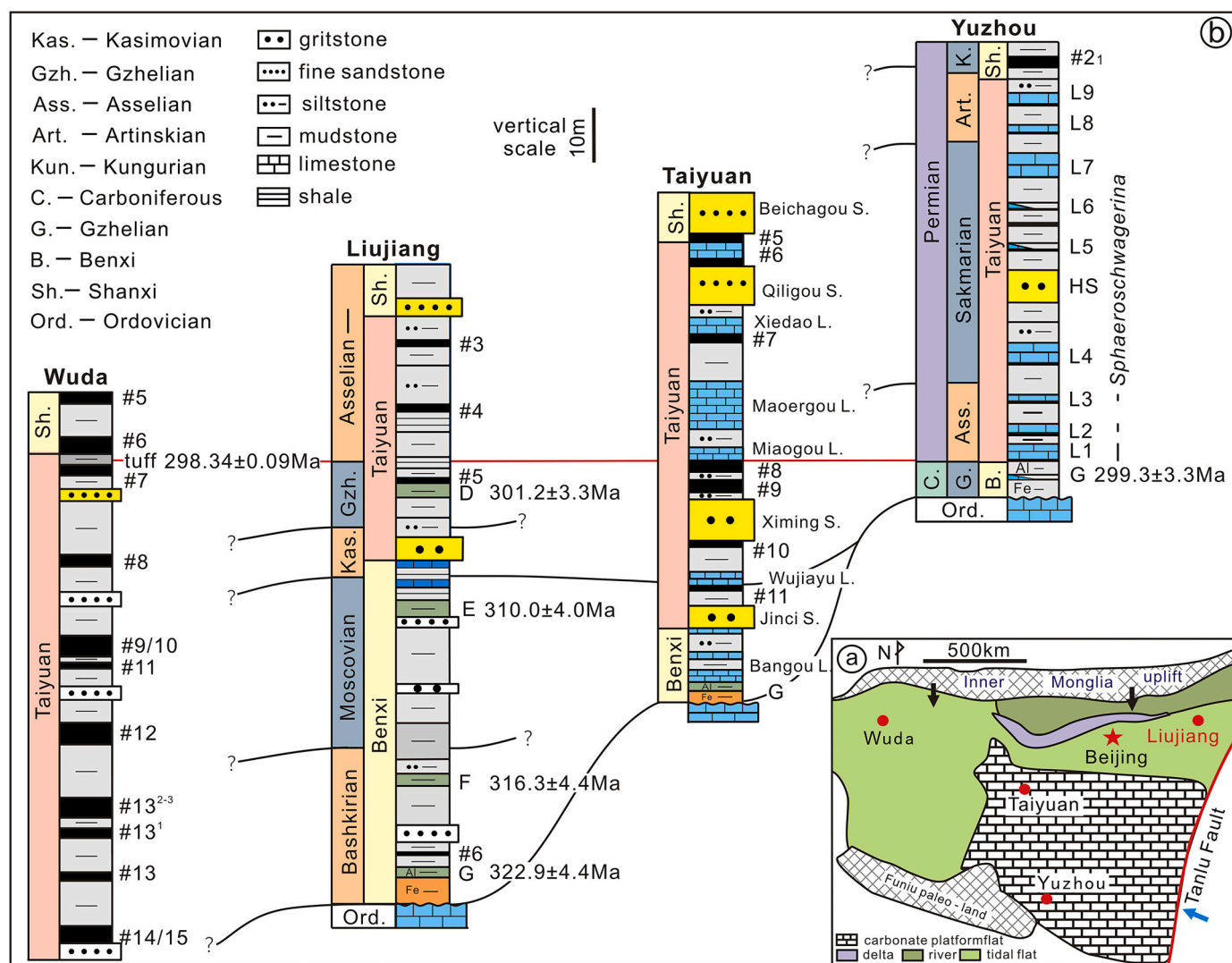

Fig. 6. a, Outline map of the North China Plate during the Pennsylvanian-Cisuralian showing the position of the Yuzhoum, Xishan, Taiyuan, Liujiang and Wuda locations, the black arrow represents the direction of source. b, Stratigraphic correlation of the diachronous sediments of the Benxi and Taiyuan formation in the North China Plate, the black lines are the boundaries of the stages.

plant growth recommenced in swampy conditions to build up biomass to form overlying #6 coal. The Wuda Tuff and has euhedral, zoned, magmatic zircon crystals that have been dated to 298.34 ± 0.09 Ma in the earliest Permian (Schmidt et al., 2020), thus providing a total age range including analytical error of 298.43–298.25 Ma. At Wuda, other thin, mm–cm scaled tuff horizons occur in the #7 and #6 coal seams, indicating episodic eruptions occurred through peat formation (Schmidt et al., 2020).

Bed 28 in the Liujiang Coalfield (Fig. 6) is a 20–25 cm thick claystone that represents altered feldspars from an air-fall tuff, and has small, euhedral, magmatic zircon crystals 50–200 μm long. Although it does not contain fossil plants like the Wuda tuff, it occurs at the base of the #5 coal seam (Bed 29) that developd in swamp conditions. The overlying Bed 30 is a greyish-black mudstone with abundant fossil plants that represents the termination of peat-forming swamp conditions. Bed 28 is here dated to 301.2 ± 3.3 Ma and as such provides a total age range of 304.5–297.9 Ma including analytical error and as such overlaps with the age of the Wuda tuff. It is possible that the two dated horizons may represent ash from the same volcanic eruption, but the other thin ashes present in the coals above and below the main Wuda tuff bed indicate frequent ashfall events at this time, from which the Bed 28 in the Liujiang coal field could conceivably correlate with one of these other tuffs. More precise dating for the Luijiang samples is required to provide more acurate stratigraphic framework, noting it has a broader error range than the Wuda tuff. Dating the smaller ash horizons in the Wuda coalfield might also provide additional information on the frequency of eruptions.

The IMU on the northern margin of the NCP was uplifted through the late Pennsylvanian and early Cisuralian, but according to Shang (1997) the terrain in the NCP was lower in the north and higher in the south, with sedimentary strata thicker in the north and thinning southerly. The Benxi and Taiyuan formations deposited during this stratigraphic interval are diachronous (Fig. 6b) with sedimentary facies migrating over time across the NCP from the NW to SE (Shang, 1997). During the late Pennsylvanian, seawater invaded the platform from the Qilian Sea in the western margin of the NCP (Shang, 1997). Through the Carboniferous-Permian transition, the topography of the NCP was reversed due to tectonic activity, resulting in topographic high in the north and topographic low in the south. During the latest Carboniferous, there was a transition in transgression direction (blue arrow in Fig. 6a), with seawater withdrawn from the basin and marine sediments exposed. Swamp conditions were widespread throughout the basin at this time, forming the #8/9 coal in the Xishan Coalfield (Taiyuan) that is equivalent to the #6/7 coal seam in the Wuda Coalfield (Fig. 6b). During the early Permian, a minor transgression occurred represented by the Miaogou Limestone in the Taiyuan Coalfield and the L1 Limestone in the Yuzhou Coalfield (Fig. 6b) with seawater invading from the southeast and an epicontinental sea covering the basin.

Using the radiometric dates from the Liujiang and Wuda Coalfields to confidently revise the stratigraphic framework, the C-P boundary is at different positions within the Benxi and Taiyuan formations depending on location. In northwestern parts of the basin, the C-P boundary occurs at the top of the Taiyuan Formation (e.g., Wuda in Fig. 6b) such that the majority of the Taiyuan Formation was deposited during the Carboniferous. In northeastern (e.g., Liujiang in Fig. 6b) and central parts of the NCP (Taiyuan in Fig. 6b), the C-P boundary occurs in the lower to middle part of the Taiyuan Formation such that it was deposited through the C-P transition. In contrast, in southwest parts of the basin such as the Yuzhou Coalfield, the C-P boundary occurs at the base of the Taiyuan Formation which was deposited entirely within the Permian (Fig. 6b). The radiometric dates add confidence to previous stratigraphical correlations that infer similar patterns (Liu et al., 2014; Schmidt et al., 2020; Yang et al., 2020).

5.2. Reliability of Hg/TOC as a proxy for volcanism

The volcanic intensity curve inferred from the Hg/TOC ratios is shown in Fig. 7a and includes four significant peaks in volcanic activity (numbered VA-I to VA-IV), intervals of weak volcanic activity during the early-middle Bashkirian and early-middle Moscovian, and an interval of fluctuating but overall long-term increasing intensity from the middle Kasimovian to the Gzhelian (Fig. 7a).

The reliability of the volcanic curve inferred from the Hg/TOC ratio can be confirmed by the relationship between the $\delta^{13}C_{org}$ and Hg/TOC ratios. Under the stable condition in organic matter and plant assemblage, terrestrial organic carbon isotopes record changes in the composition of CO_2 of ancient atmospheres and is, therefore, an effective proxy (Wang, 2010; Vervoort et al., 2019). Volcanic activity comprises eruptions and intrusions and releases large amounts of comparatively isotopically heavy CO_2 (−5‰ to −8‰, Javoy et al., 1986) and Hg, resulting in Hg enrichment and increasing atmospheric pCO_2 (Grasby et al., 2019; Vervoort et al., 2019). Magma intrusion into organic-rich sediments including mudrocks, peat, coal and petroleum reservoirs releases massive volumes of ^{13}C-depleted CO_2 (−22‰), CH_4 (−60‰) and a large amounts of Hg (Grasby et al., 2019; Vervoort et al., 2019); these would result in Hg enrichment, increasing atmospheric pCO_2 and decreasing $\delta^{13}C$ values in coeval atmospheres (McElwain et al., 2005).

In the study area, four peaks in volcanic activity (VA-I, VA-II, VA-III, and VA-IV) correspond to the four negative excursions of $\delta^{13}C_{org}$ (CIE-I, CIE-II, CIE-III, and CIE-IV), suggesting a common source in heating of organic-rich sediments by magma intrusion (Shen et al., 2019b). The negative coupling correlation of the Hg/TOC and $\delta^{13}C_{org}$ curves from the Bashkirian to early Gzhelian support the above conclusion. However, this relationship becomes decoupled from the middle to late Gzhelian (Fig. 7a, b), the cause of which may be related to the stronger volcanic eruptions releasing large amounts of relatively heavy CO_2 (−6%) into the atmosphere. This inference is consistent with contemporaneous increasing atmospheric CO_2 concentration (Foster et al., 2017; Fig. 7c) and widely records of the extrusive igneous rocks (Torsvik et al., 2008). At the same time, atmospheric CO_2 concentration increase during the late Kasimovian to Gzhelian may also be related to concurrent reduction in tropical forest area (Fig. 7f) and the weakening of atmospheric CO_2 consumption by weathering.

Pennsylvanian volcanism recorded in the literature lends some support to the inferred volcanic activity curve in the study area. During the Pennsylvanian, volcanism was globally widespread with centers in the northern margin of the NCP, NW Europe, the northwestern Tarim Plate, and the northern margin of Gondwana (Chen and Xu, 2019), with intensities increasing towards the Carboniferous-Permian boundary (Fig. 7a). So far, no large volcanic events have been identified that correspond to the stratigraphic position of VA-I other than suites of intrusive rocks from the Pennsylvania to earliest Cisuralian (315–297 Ma) in the northern margin of the NCP. Magma emplacement may have intruded into organic rich strata from the stratigraphically older Carboniferous strata (Zhang et al., 2009). The commencement of the magma intrusion roughly corresponds to the position of volcanic peak VA-I in the study area during the late Bashkirian (Fig. 7).

In NW Europe, zircon ages from volcanism in Germany identify peaks of activity at ~300 Ma and ~307 Ma (Torsvik et al., 2008). The volcanism at ~307 Ma during the latest Moscovian coincides with magma intrusion in the northern part of the NCP at ~306–308 Ma (Zhang et al., 2009). These volcanic events may have heated overlying organic-rich sediments, leading to the release of isotopically light carbon as recorded in volcanic peak VA-II in the study area. From the Kasimovian to Gzhelian, the intensity of volcanic activity inferred from the Hg/TOC ratios fluctuates but shows an overall increasing trend towards the Permian boundary. This includes two negative carbon isotope excursions in the early Gzhelian and at the Carboniferous–Permian boundary coincide with peaks in volcanic intensity (VA-III and VA-IV; Fig. 7a, b). Such a trend of increasing volcanism is consistent with the
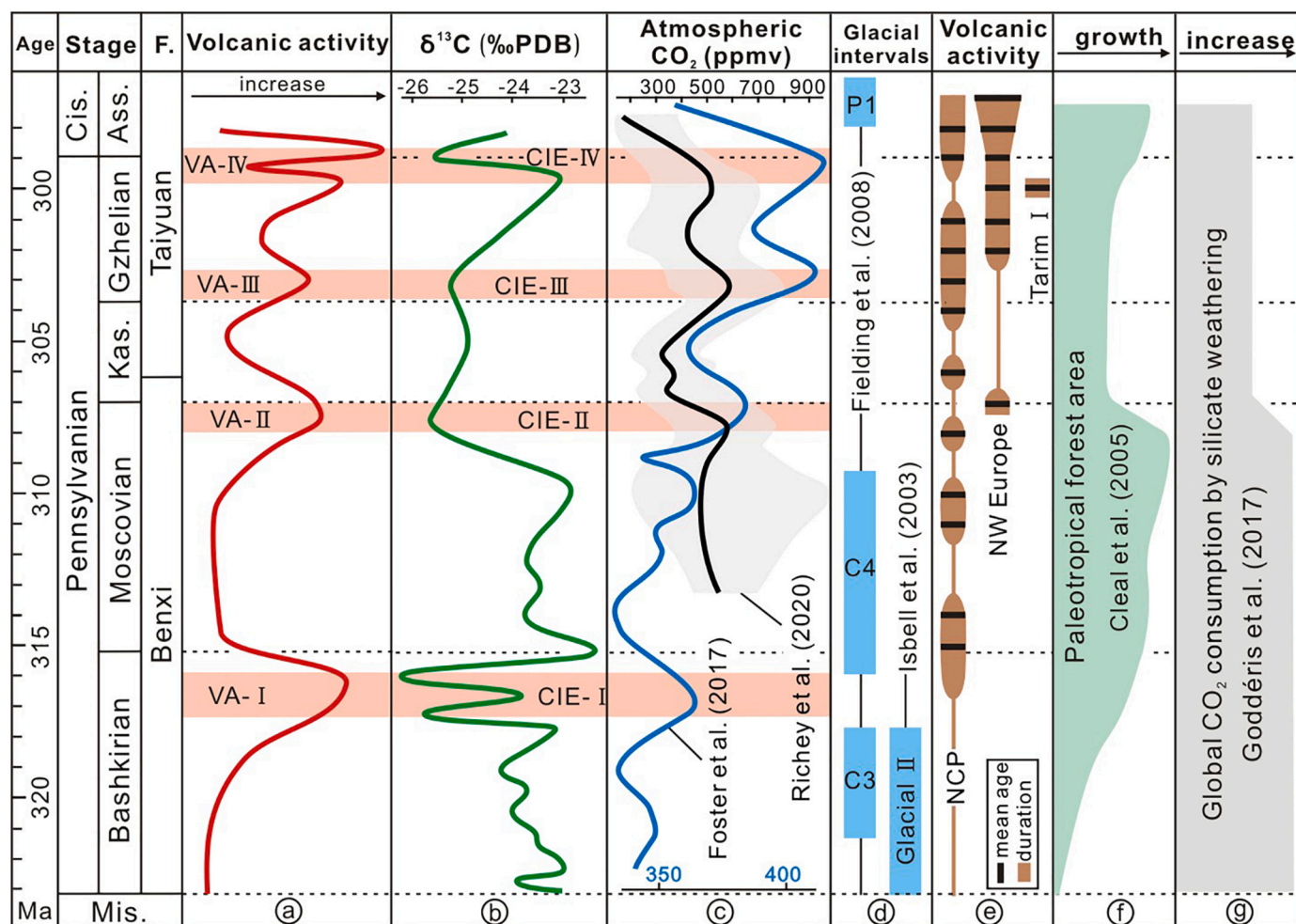
Fig. 7. Correlation of Pennsylvanian-earliest Cisuralian global events. a, Volcanic activity from this study. b, $\delta^{13}C$ variation from this study. c, Atmospheric CO_2 from Foster et al. (2017) and Richey et al. (2020). d, Glacial intervals from Fielding et al. (2008) and Isbell et al. (2003). e, Timing of volcanic activity. Data from the northern NCP from Zhang et al. (2009 and the references therein), Europe (Germany) from Torsvik et al. (2008) and Tarim I from Xu et al. (2014). f, Paleotropical forest extent from Cleal and Thomas (2005). g, Global CO_2 consumption by silicate weathering from Goddéris et al. (2017). Abbreviations: Cis. – Cisuralian, Mis. - Mississippian, Ass. – Asselian, Kas. - Kasimovian.

extensive development of volcanism triggered by the collision and subduction of global plates along with the arrival of the assembly peak of Pangea (Zhao et al., 2018). VA-III is most likely related to the volcanic activity from the northern NCP and NW Europe, and VA-IV is most likely related to the combination of volcanic activity from intrusions in the northern NCP, extrusive lavas in the Skagerrak-Centered LIP and both intrusive and extrusive volcanism in the northwestern Tarim Plate (~300–298 Ma; Torsvik et al., 2008; Zhang et al., 2009; Xu et al., 2014).

In the Liujiang Coalfield, all of the tuffaceous claystone horizons have low Hg values, typically from 0 to 25 ppb (Fig. 4a). Only sample LJ F from bed 12 in the late Bashkirian occurs within the stratigraphic range of a carbon isotope excursion or volvanic activity peak, in this case occuring within the range of CIE-I/VA-I. This suggests that overall, the individual tuffaceous claystones did not not contribute significantly to the input of Hg into terrestrial settings for these particular beds, and that the Hg peaks relate to other volcanic events. We consider the likely source of the ash in the tuffaceous claystones is from extrusive volcanism in the northern part of the NCP (Zhang et al., 2009) and that Hg deposition in the studied section may represents a global rather than local phenomenon (Sanei et al., 2012; Blum et al., 2014).

5.3. Volcanism and $\delta^{13}C$ values linked to atmospheric pCO_2 and palaeoclimate

Volcanic activity, palaeotropical lowland "coal" forests and the extent of silicate weathering are considered dominant factors controlling atmospheric pCO_2 and climate change during the Pennsylvanian (Cleal and Thomas, 2005; Goddéris et al., 2017; Yang et al., 2020). Past research has inferred phases of glacial activity during the Phanerozoic from secular patterns in $\delta^{13}C$ values from marine carbonates (Grossman et al., 2008; Liu et al., 2017). Ice-age conditions during the Carboniferous and Permian have been inferred based on generally higher $\delta^{13}C$ and $\delta^{18}O$ values relative to adjacent time intervals (Veizer et al., 1999). In the study area, the carbon isotope values show positive plateaus during the early-middle Bashkirian that corresponds to the C3 glacial of Fielding et al. (2008) and glacial interval II of Isbell et al. (2003) (Fig. 7d), while the plateau in the early-middle Moscovian corresponds to glacial interval C4 of Fielding et al. (2008). These glacial intervals are separated by a period of increased volcanism (VA-I) and its corresponding negative carbon isotope excursion (CIE-I; Fig. 7d) in the late Bashkirian. Contemporaneous with coeval volcanism peak VA-I in the study area (Fig. 7a), increases in pCO_2 values (Fig. 7c; Foster et al., 2017) show that volcanism is one of the main drivers for the increased atmospheric pCO_2 and climate warming during the warm interglacial between the C3 and C4 glacials.

During the late Moscovian–Gzhelian in the study area, carbon isotope trends show a fast negative excursion (CIE-II) followed by stable increasing values, corresponding to the interglacial between the C2 and P1 glaciations in Australia (Fig. 7d; Fielding et al., 2008). Volcanic peak VA-II and VA- III during the late Moscovian and early Gzhelian, along with the increase of pCO$_2$ (Fig. 7c; Foster et al., 2017; Richey et al., 2020), show that volcanism was one of the main drivers for the increased atmospheric pCO$_2$ and the climate warming shift from glacial conditions during the Bashkirian–Moscovian to interglacial conditions during the Kasimovian–Gzhelian (Davydov et al., 2013; Davydov and Biakov, 2015; Yang et al., 2020). This coincided with the rapid contraction of tropical "coal" forest area caused by the Hercynian orogeny (~53%) (Fig. 7f; Cleal and Thomas, 2005; Hilton and Cleal, 2007).

During the middle to late Gzhelian, positive carbon isotope excursions in the study area and the Youjiang (South China), Naqing (South China), Kongshan (East China) and Russian Moscow profiles (Liu et al., 2017; Buggisch et al., 2011; Grossman et al., 2008), may be attribute to the enhanced volcanic activity during this interval that released large amounts of relatively heavy CO$_2$ (−6%) into atmospheres to make atmosphere CO$_2$ heavier, consistent with the increase of pCO$_2$.

Volcanic peak VA-IV spanning the C-P transition corresponds to negative excursion CIE-IV and is accompanied by an increase in pCO$_2$ (Fig. 7c; Foster et al., 2017; Richey et al., 2020). This suggests that this interval of climate warming during Carboniferous-Permian icehouse correlates with periods of volcanic activity. The emplacement of the Skagerrak-Centered Large Igneous Province and the Tarim Large Igneous Province as well as volcanism in the NCP are likely culprits (Fig. 7e; Torsvik et al., 2008, Xu et al., 2014). These events are likely to have released voluminous CO$_2$ emissions that led to climate warming (Fig. 7c; Foster et al., 2017; Richey et al., 2020). This is immediately followed cooling during the earliest Permian that may have been the result of rapid post-eruptional weathering of the recently formed basaltic rocks in tropical latitudes, which would have sequestered atmospheric CO$_2$ and promoted return to cooler icehouse conditions (Yang et al., 2020).

6. Conclusion

(1) Four tuffaceous claystone horizons were dated using zircon U-Pb methods, yielding ages of 322.7 ± 3.1 Ma, 316.3 ± 4.4 Ma, 310.0 ± 4.0 Ma and 301.2 ± 3.3 Ma. The new dates allow for a chronostratigraphic model for the target strata in the Benxi and Taiyuan formations from the Liujiang Coalfield to be developed. This constrains the studied section to ~322 Ma to 301 Ma and allows mean depositional rates for the lower (2.81 m/Myr) and upper parts (5.55 m/Myr) of the Benxi Formation and the upper Benxi Formatin to the early Taiyuan Formation (2.84 m/Myr) to be determined.

(2) Hg/TOC ratios vary from 9.98 ppb/% to 198.88 ppb/% ($\bar{x}$ = 53.77 ppb/%) and include four peaks (VA-I, VA-II, VA-III, and VA-IV) that record increased volcanic intensity during the late Bashkirian, the late Moscovian, early Gzhelian, and through the C-P transition period. Two low ebbs of Hg/TOC values during the early-middle Bashkirian and the early-middle Moscovian indicate periods with low volcanic influence.

(3) δ^{13}C$_{org}$ values vary from −26.4‰ to −22.3‰ ($\bar{x}$ = −24.3‰) and present four negative excursions of about 3.8‰ (CIE-I), 3.4‰ (CIE-II), 0.4‰ (CIE-III) and 2.6‰ (CIE-IV). Vertically through the succession δ^{13}C$_{org}$ values include positive isotope plateaus in the late-middle Bashkirian and late-middle Moscovian, and a stable increasing trend separated by a negative excursion during the Kasimovian–Gzhelian.

(4) Hg/TOC ratios peaks of volcanic intensity VA-I, VA-II, VA-III, and VA-IV coincide with the the negative carbon isotope excursions CIE -I, CIE -II, CIE -III, and CIE -IVand also intervals of high

atmospheric pCO$_2$ and the interglacial intervals. We consider volcanism to be one of the dominant drivers for changes of atmospheric pCO$_2$ and climate warming during Pennsylvanian interglacials. The two lower ebbs correlate with the two positive isotope plateaus, intervals of lower atmospheric pCO$_2$ concentration and global cooling causing glacial intervals C3 and C4, and suggest low volcanic influences at these times.

(5) Our data adds further support to volcanism as a causal mechanism for increasing atmospheric pCO$_2$ and driving the global climate cycles from glacial to interglacial through greenhouse gas emissions in the Paleozoic.

Declaration of Competing Interest

The authors declare that they have no known competing financial interests or personal relationships that could have appeared to influence the work reported in this paper.

References

Blakey, R., 2011. Mollewide plate tectonic maps, Colorado Plateau geosystems. World Wide Web address. http://cpgeosystems.com/mollglobe.html (accessed 15.11. 2015).

Blum, J.D., Sherman, L.S., Johnson, M.W., 2014. Mercury isotopes in earth and environmental sciences. Annu. Rev. Earth Planet. Sci. Lett. 42, 249–269.

Bond, D.P.G., Grasby, S.E., 2017. On the causes of mass extinctions. Palaeogeogr. Palaeoclimatol. Palaeoecol. 478, 3–29.

Buggisch, W., Wang, X., Alekseev, A.S., Joachimski, M.M., 2011. Carboniferous–Permian carbon isotope stratigraphy of successions from China (Yangtze platform), USA (Kansas) and Russia (Moscow Basin and the Urals). Palaeogeogr. Palaeoclimatol. Palaeoecol. 301 (1–4), 18–38.

Chen, J., Xu, Y., 2019. Establishing the link between Permian volcanism and biodiversity changes: Insights from geochemical proxies. Gondwana Res. 75, 68–96. https://doi.org/10.1016/j.gr.2019.04.008.

Chu, D.L., Grasby, S.E., Song, H.J., Dal Corso, J., Wang, Y., Mather, T.A., Wu, Y., Song, H. Y., Shu, W.C., Tong, J.N., Wignall, P.B., 2020. Ecological disturbance in tropical peatlands prior to marine Permian-Triassic mass extinction. Geology 48, 288–292. https://doi.org/10.1130/g46631.1.

Cleal, C.J., Thomas, 2005. Palaeozoic tropical rainforests and their effect on global climates: is the past the key to the present? Geobiology 3, 13–31. https://doi.org/10.1111/j.1472-4669.2005. 00043.X.

Davydov, V.I., Biakov, A.S., 2015. Discovery of shallow-marine biofacies conodonts in a bioherm within the Carboniferous-Permian transition in the Omolon Massif, NE Russia near the North Paleo-pole: correlation with a warming spike in the southern hemisphere. Gondwana Res. 28, 888–897.

Davydov, V.I., Haig, D.W., McCartain, E., 2013. A latest Carboniferous warming spike recorded by a fusulinid-rich bioherm in Timor Leste: Implications for East Gondwana deglaciation. Palaeogeogr. Palaeoclimatol. Palaeoecol. 376, 22–38.

Dong, Y., Santosh, M., 2016. Tectonic architecture and multiple orogeny of the Qinling Orogenic Belt, Central China. Gondwana Res. 29, 1–40. https://doi.org/10.1016/j.gr.2015.06.009.

Faure, K., de Wit, M.J., Willis, J.P., 1995. Late Permian global coal hiatus linked to 13^{C}-depleted CO$_2$ flux into the atmosphere during the final consolidation of Pangea. Geology 23 (6), 507–510.

Fielding, C.R., Frank, T.D., Birgenheier, L.P., Rygel, M.C., Jones, A.T., Roberts, J., 2008. Stratigraphic imprint of the late Paleozoic Ice Age in eastern Australia: a record of alternating glacial and nonglacial climate regime. J. Geol. Soc. Lond. 165, 129–140.

Foster, G.L., Royer, D.L., Lunt, D.J., 2017. Future climate forcing potentially without precedent in the last 420 million years. Nature Comms 8, 14845.

Goddéris, Y., Donnadieu, Y., Carretier, S., Aretz, M., Dera, G., Macouin, Mélina, 2017. Onset and ending of the late Palaeozoic ice age triggered by tectonically paced rock weathering. Nat. Geosci. 10 (5), 382–386.

Grasby, S.E., Sanei, H., Beauchamp, B., Chen, Z., 2013. Mercury deposition through the Permo–Triassic biotic crisis. Chem. Geol. 351, 209–216.

Grasby, S.E., Them, T.R., Chen, Z., Yin, R., Ardakani, O.H., 2019. Mercury as a proxy for volcanic emissions in the geologic record. Earth-Sci. Rev. 196, 102880. https://doi.org/10.1016/j.earscirev.2019.102880.

Grossman, E.L., Yancey, T.E., Jones, T.E., Bruckschen, P., Chuvashov, B., Mazzullo, S.J., Mii, H., 2008. Glaciation, aridification, and carbon sequestration in the Permo-Carboniferous: the isotopic record from low latitudes. Palaeogeogr. Palaeoclimatol. Palaeoecol. 268, 222–233. https://doi.org/10.1016/j.palaeo.2008.03.053.

Hilton, J., Cleal, C.J., 2007. The relationship between Euramerican and Cathaysian tropical floras in the late Palaeozoic: palaeobiogeographical and palaeogeographical implications. Earth-Sci. Rev. 85, 85–116.

Hu, F.Z., Fu, X.G., Lin, L., Song, C.Y., Wang, Z.W., Tian, K.Z., 2020. Marine late Triassic-Jurassic carbon-isotope excursion and biological extinction records: New evidence from the Qiangtang Basin, eastern Tethys. Glob. Planet. Chang. 185, 103093. https://doi.org/10.1016/j.gloplacha.2019.103093.

Isbell, J.L., Miller, M.F., Wolfe, K.L., Lenaker, P.A., 2003. Timing of late Paleozoic glaciation in Gondwana: was glaciation responsible for the development of Northern Hemisphere cyclothems? Extreme Deposit. Environm. Mega End Memb. Geol. Time Spec. Paper 370, 5–24.

Javoy, M., Pineau, F., Delorme, H., 1986. Carbon and nitrogen isotopes in the mantle. Chem. Geol. 57 (1–2), 41–62.

Liao, Z.W., Hu, W.X., Cao, J., Wang, X.L., Yao, S.P., Wu, H.G., Wan, Y., 2016. Permian-Triassic boundary (PTB) in the lower Yangtze Region, southeastern China: a new discovery of deep-water archive based on organic carbon isotopic and U-Pb geochronological studies. Palaeogeogr. Palaeoclimatol. Palaeoecol. 451, 124–139. https://doi.org/10.1016/j.palaeo.2016.03.004.

Liu, C., Jarochowska, E., Du, Y., Vachard, D., Munnecke, A., 2017. Stratigraphical and $\delta^{13}C$ records of Permo-Carboniferous platform carbonates, South China: responses to late Paleozoic icehouse climate and icehouse–greenhouse transition. Palaeogeogr. Palaeoclimatol. Palaeoecol. 474, 113–129. https://doi.org/10.1016/j.palaeo.2017.06.038.

Liu, J., Zhao, Y., Liu, A., Zhang, S., Yang, Z., Zhuo, S., 2014. Origin of late Palaeozoic bauxites in the North China Craton: constraints from zircon U–Pb geochronology and in situ Hf isotopes. J. Geol. Soc. 171, 695–707. https://doi.org/10.1144/jgs2013-074.

McElwain, J.C., Wade-Murphy, J., Hesselbo, S.P., 2005. Changes in carbon dioxide during an oceanic anoxic event linked to intrusion into Gondwana coals. Nature 435 (7041), 479–482.

Montañez, I., Deb, N.J.T., Tracy, F., Christopher, F., Isbell, J.L., Birgenheier, L.P., Rygel, M.C., 2007. CO2-forced climate and vegetation instability during late Paleozoic deglaciation. Science 315, 87–91. https://doi.org/10.1029/2003JD003660.

Montañez, I.P., McElwain, J.C., Poulsen, C.J., White, J.D., DiMichele, W.A., Wilson, J.P., Griggs, G., Hren, M.T., 2016. Climate, pCO2 and terrestrial carbon cycle linkages during late Palaeozoic glacial–interglacial cycles. Nat. Geosci. 9, 1–5.

Peng, Y.J., Chen, Y.J., Liu, Y.W., 2003. Benxi formation - lithohorizon and chronohorizon with diachronism. Global Geol. 22, 111–118 (in Chinese with English abstract).

Percival, L.M., Ruhl, M., Hesselbo, S.P., Jenkyns, H.C., Mather, T.A., Whiteside, J.H., 2017. Mercury evidence for pulsed volcanism during the end-Triassic mass extinction. Proc. Natl. Acad. Sci. U. S. A. 114 (30), 7929–7934.

Pyle, D.M., Mather, T.A., 2003. The importance of volcanic emissions for the global atmospheric mercury cycle. Atmos. Environ. 37 (36), 5115–5124.

Richey, J.D., Montañez, I.P., Goddéris, Y., Looy, C.V., Griffis, N.P., DiMichele, W.A., 2020. Influence of temporally varying weatherability on CO2-climate coupling and ecosystem change in the late Paleozoic. Clim. Past 16, 1759–1775. https://doi.org/10.5194/cp-16-1759-2020.

Sanei, H., Grasby, S.E., Beauchamp, B., 2012. Latest Permian mercury anomalies. Geology 40 (1), 63–66.

Schmidt, M.D., Pfefferkorn, H.W., Shen, S.Z., Wang, J., 2020. A volcanic tuff near the Carboniferous-Permian boundary, Taiyuan Formation, North China: radioscopic dating and global correlation. Rev. Palaeobot. Palynol. 6, 1–6.

Shang, G., 1997. The Late Paleozoic Coal Geology of North China Platform. Shanxi Science and Technology Press, Taiyuan, pp. 1–160.

Shen, J., Algeo, T.J., Chen, J., Planavsky, N.J., Feng, Q., Yu, J., Liu, J., 2019a. Mercury in marine Ordovician/Silurian boundary sections of South China is sulfide-hosted and non-volcanic in origin. Earth Planet. Sci. Lett. 511, 130–140. https://doi.org/10.1016/j.epsl.2019.01.028.

Shen, J., Yu, J., Chen, J., Algeo, T.J., Xu, G., Feng, Q., Shi, X., Planavsky, N.J., Shu, W., Xie, S., 2019b. Mercury evidence of intense volcanic effects on land during the Permian-Triassic transition. Geology 47. https://doi.org/10.1130/G46679.1.

Shen, J., Feng, Q., Algeo, T.J., Liu, J., Zhou, C., Wei, W., Liu, J., Them, T.R., Gill, B.C., Chen, J., 2020. Sedimentary host phases of mercury (Hg) and implications for use of Hg as a volcanic proxy. Earth Planet. Sci. Lett. 543, 116333. https://doi.org/10.1016/j.epsl.2020.116333.

Sláma, J., Košler, J., Condon, D.J., Crowley, J.L., Gerdes, A., Hanchar, J.M., Horstwood, M.S., Morris, G.A., Nasdala, L., Norberg, N., 2008. Plešovice zircon - a new natural reference material for U–Pb and Hf isotopic microanalysis. Chem. Geol. 249 (1–2), 1–35.

Soreghan, G.S., Soreghan, M.J., Heavens, N.G., 2019. Explosive volcanism as a key driver of the late Paleozoic ice age. Geology 47, 600–604. https://doi.org/10.1130/G46349.1.

Torsvik, T.H., Smethurst, M.A., Burke, K., Steinberger, B., 2008. Long term stability in deep mantle structure: evidence from the ~300 Ma Skagerrak-Centered large Igneous Province (the SCLIP). Earth Planet. Sci. Lett. 267, 444–452.

Veizer, J., Ala, D., Azmy, K., Bruckschen, P., Buhl, D., Bruhn, F., Carden, G.A.F., Diener, A., Ebneth, S., Godderis, Y., Jasper, T., Korte, C., Pawellek, F., Podlaha, O.G., Strauss, H., 1999. $^{87}Sr/^{86}Sr$, $\delta^{13}C$ and $\delta^{18}O$ evolution of Phanerozoic seawater in earth system evolution. Chem. Geol. 161, 59–88.

Vervoort, P., Adloff, M., Greene, S.E., Kirtland Turner, S., 2019. Negative carbon isotope excursions: an interpretive framework. Environ. Res. Lett. 14, 85014. https://doi.org/10.1088/1748-9326/ab3318.

Wang, J., 2010. Late Paleozoic macrofloral assemblages from Weibei Coalfield, with reference to vegetational change through the late Paleozoic Ice-age in the North China Block. Int. J. Coal Geol. 83, 292–317. https://doi.org/10.1016/j.coal.2009.10.007.

Wang, J., Pfefferkorn, H.W., Zhang, Y., Feng, Z., 2012. Permian vegetational Pompeii from Inner Mongolia and its implications for landscape paleoecology and paleobiogeography of Cathaysia. Proc. Natl. Acad. Sci. U. S. A. 109, 4927–4932. https://doi.org/10.1073/pnas.1115076109.

Wang, X., Cawood, P.A., Zhao, H., Zhao, L., Grasby, S.E., Chen, Z., Zhang, L., 2019. Global mercury cycle during the end-Permian mass extinction and subsequent early Triassic recovery. Earth Planet. Sci. Lett. 513, 144–155. https://doi.org/10.1016/j.epsl.2019.02.026.

Wiedenbeck, M., Alle, P., Corfu, F., Griffin, W.L., Meier, M., Oberli, F., Vonquadt, A., Roddick, J.C., Spiegel, W., 1995. Three natural Zircon standards for U-Th-Pb, Lu-Hf, trace-element and ree analyses. Geostand. Newslett. 19 (1), 1–23.

Wiedenbeck, M., Hanchar, J.M., Peck, W.H., Sylvester, P., Valley, J., Whitehouse, M., Kronz, A., Morishita, Y., Nasdala, L., Fiebig, J., Franchi, I., Girard, J.P., Greenwood, R.C., Hinton, R., Kita, N., Mason, P.R.D., Norman, M., Ogasawara, M., Piccoli, P.M., Rhede, D., Satoh, H., Schulz-Dobrick, B., Skår, Ø., Spicuzza, M.J., Terada, K., Tindle, A., Togashi, S., Vennemann, T., Xie, Q., Zheng, Y.-F., 2004. Further characterisation of the 91500 zircon crystal. Geostand. Geoanal. Res. 28 (1), 9–39.

Xu, Y.G., Wei, X., Luo, Z.Y., Liu, H.Q., Cao, J., 2014. The early Permian Tarim large Igneous Province: Main characteristics and a plume incubation model. Lithos 204, 20–35.

Yang, J., Cawood, P.A., Montañez, I.P., Condon, D.J., Du, Y., Yan, J., Yan, S., Yuan, D., 2020. Enhanced continental weathering and large igneous province induced climate warming at the Permo-Carboniferous transition. Earth Planet. Sci. Lett. 534, 116074.

Yin, H., Feng, Q., Lai, X., Baud, A., Tong, J., 2007. The protracted Permo-Triassic crisis and multi-episode extinction around the Permian-Triassic boundary. Glob. Planet. Chang. 55, 1–20.

Zhang, S.H., Zhao, Y., Kroener, A., Liu, X.M., Xie, L.W., Chen, F.K., 2009. Early Permian plutons from the northern North China block: constraints on continental arc evolution and convergent margin magmatism related to the central Asian orogenic belt. Int. J. Earth Sci. 98 (6), 1441–1467.

Zhang, S.H., Zhao, Y., Ye, H., Liu, J.M., Hu, Z.C., 2014. Origin and evolution of the Bainaimiao arc belt: Implications for crustal growth in the southern Central Asian orogenic belt. Geol. Soc. Am. Bull. 126, 1275–1300. https://doi.org/10.1130/B31042.1.

Zhao, G., Wang, Y., Huang, B., Dong, Y., Lie, S., Zhang, G., Yu, S., 2018. Geological reconstructions of the East Asian blocks: from the breakup of Rodinia to the assembly of Pangea. Earth Sci. Rev. 186, 262–286. https://doi.org/10.1016/j.earscirev.2018.10.003.

Zhong, R., Sun, S., 1996. Sedimentary characteristics and temporal and spatial distribution of volcanic events in Benxi Formation and Taiyuan formation, North China platform. Acta Geomech. 2 (1), 83–91.